Optimization of EUV laser and discharge devices for high-volume manufacturing

A. Hassanein*, V. Sizyuk, T. Sizyuk, and V. Morozov
Argonne National Laboratory, 9700 South Cass Ave, Argonne, IL, USA

ABSTRACT

Both Laser and Discharge produced plasma (LPP and DPP) are being used as a light source for EUV lithography. A key challenge for the EUV radiation plasma devices is achieving sufficient brightness to support the throughput requirements of High-Volume Manufacturing lithography exposure tools. One method for improving source brightness is to simulate the source environment in order to optimize the EUV output. An integrated model for the description of hydrodynamics and optical processes in DPP and LPP devices has been developed and integrated into the HEIGHTS–EUV computer simulation package. Model development consisted of several main tasks: plasma evolution and magnetohydrodynamic (MHD) processes; detailed photon radiation transport, and physics of plasma/electrode interactions in DPP devices, scattering processes of the neutral and charged particles of plasma. Advanced numerical methods for the description of magnetic compression and diffusion in 2D and 3D geometries are used in the HEIGHTS package. Radiation transport of both continuum and lines is taken into account with detailed spectral profiles in the EUV region. Monte Carlo methods are used for the modeling of the radiation transport processes, laser radiation absorption, and the debris particles behavior in magnetic field.

Keywords: HEIGHTS, discharge produced plasma, laser produced plasma, EUV radiation, computer simulation, MHD, Monte Carlo method.

1. INTRODUCTION

The EUV lithography community has made several important developments to improve EUV radiation source devices. Recent advances in laser and discharge systems with high repetition rate and high average power suggest the feasibility of modular, flexible, and relatively inexpensive microelectronic production facilities based on laser and discharge plasma sources. However, several challenges remain. Modern projection lithography systems require [1] as a minimum 1% conversion efficiency of laser light into soft X-rays within a 2% bandwidth at 13.5 nm wavelength, where multilayer reflectivity of more than 60% can be routinely achieved by Mo-Si mirrors. Final in-band power must be obtained, with an intermediate focus over 120 W. These requirements necessitate investigation and optimization not only of power sources but also plasma irradiation parameters, plasma energy deposition, target material, device design, debris mitigation etc. In this work, we present our simulation model of the MHD, optical processes, and the plasma particles interaction that occurs in DPP and LPP devices.

For that purpose, an integrated MHD model and its base HEIGHTS package [2-4] are used. The model considers five main processes: laser radiation absorption, plasma evolution by generation of a magnetic field, radiation transport, EUV generation in the 13.5-nm diapason, and the plasma debris interaction. The integrated model uses the total variation diminishing (TVD) scheme in the Lax-Friedrich formulation [5, 6] for the description of the laser produced plasma motion, an implicit scheme with sparse matrix solver for heat transport and magnetic diffusion processes, and weighted Monte Carlo model [7, 8] for radiation transport, EUV output, and the accelerated ions behavior simulation. Several models [9] are being developed and can be used to calculate opacity. A collisional radiation equilibrium (CRE) model is used in this case, which is a self-consistent model that takes into account Auger processes, and a nonstationary kinetic model that depends on the complexity of the problem as well as the availability of computer time. Different sets of opacities for the MHD and the EUV calculations were used: (a) 3693 spectral groups for Xe and 3240 groups for Sn in wide range, and (b) about 2500 spectral points for Xe and up to 5000 spectral points for Sn within the EUV region.

This paper describes our simulation of MHD and optical processes that occur in DPP and LPP devices in which the EUV output is an objective variable. Xenon and tin were tested as plasma source materials. Various methods of fuel delivery and discharge regimes have been investigated using the HEIGHTS integrated models. These models include utility programs for calculating EUV output and optimizing the reflection system geometry. Another important problem is the

* hassanein@anl.gov; phone (630)252-5889

Emerging Lithographic Technologies XI, edited by Michael J. Lercel,
Proc. of SPIE Vol. 6517, 65171X, (2007) · 0277-786X/07/$18
doi: 10.1117/12.712300

lifetime of the source components, in particular, that of the collector mirror reflectivity. The collector mirror lifetime is a major issue for discharge-produced and laser-produced plasma sources, where multilayer as well as single layer mirrors are used as collector systems. The collector optic lifetime noticeably decreases under the influence of plasma device debris: accelerated ions, neutral particles, and droplets [10, 11]. As a result, the EUV lithography community is actively investigating methods of debris mitigation. We present the physical models developed for simulating and optimizing a debris mitigation device based on gaseous jets and external magnetic fields. The proposed debris mitigation system includes a gaseous pipe jet for removing neutral debris and a deflecting magnetic field for deviating fast ions.

2. MATHEMATICAL MODEL

We consider the general set of three-dimensional (3D) resistive MHD equations [4] expanded with heat transport fluxes, radiation fluxes, electron-ion interaction term, and laser absorption source term. The general set of equations is presented in two-temperature approximation model:

$$
\begin{aligned}
&\frac{\partial \rho}{\partial t} + \nabla \cdot (\rho \mathbf{v}) = 0 \\
&\frac{\partial \rho \mathbf{v}}{\partial t} + \nabla \cdot \left(\rho \mathbf{v}\mathbf{v} + p_{tot} - \frac{\mathbf{B}\mathbf{B}}{4\pi\mu} \right) = -\frac{1}{4\pi\mu} \mathbf{B} (\nabla \cdot \mathbf{B}) \\
&\frac{\partial e_{tot}}{\partial t} + \nabla \cdot \left[\mathbf{v}(e_{tot} + p_{tot}) - \frac{1}{4\pi\mu} (\mathbf{v} \cdot \mathbf{B}) \cdot \mathbf{B} + \frac{c^2 \eta}{16\pi^2 \mu^2} (\nabla \times \mathbf{B}) \times \mathbf{B} - \lambda_e \nabla T_e - \lambda_i \nabla T_i - \mathbf{S}_{rad} \right] = \\
&\qquad = Q_{las} - \frac{1}{4\pi\mu} (\mathbf{v} \cdot \mathbf{B}) \cdot (\nabla \cdot \mathbf{B}) \\
&\frac{\partial e_i}{\partial t} + \nabla \cdot \left[\mathbf{v}(e_i + p_i) - \lambda_i \nabla T_i \right] = 3 \frac{m_e n_e}{m_i \tau_e} (k_B T_e - k_B T_i) \\
&\frac{\partial \mathbf{B}}{\partial t} + \nabla \cdot (\mathbf{v}\mathbf{B} - \mathbf{B}\mathbf{v}) + \frac{c^2}{4\pi\mu} \nabla \times (\eta \nabla \times \mathbf{B}) + \frac{c k_B}{e n_e} \nabla n_e \times \nabla T_e = -\mathbf{v} (\nabla \cdot \mathbf{B})
\end{aligned}
\tag{1}
$$

Here, e_{tot} – total energy that includes the hydrodynamic part, $e_h = e_e + e_i + e_{kin}$, and the magnetic part $e_m = \frac{B^2}{8\pi\mu}$; e_e – electronic component of the plasma energy that includes thermal energy of electron and ionization energy; e_i – ion component of the plasma energy; and $e_{kin} = \frac{\rho v^2}{2}$ – kinetic energy of the plasma. Analogous to energy, pressure has hydrodynamic and magnetic parts: $p_{tot} = p_e + p_i + \frac{B^2}{8\pi\mu}$. Magnetic diffusion processes are taken into account as the Joule heat term, $\frac{c^2 \eta}{16\pi^2 \mu^2} (\nabla \times \mathbf{B}) \times \mathbf{B}$, in the total energy equation and as the diffusion term, $\frac{c^2}{4\pi\mu} \nabla \times (\eta \nabla \times \mathbf{B})$, in the magnetic field equation, where η is resistivity, and μ is magnetic permeability. In the

calculations we assumed $\mu = 1$ for the plasma. The thermal conduction in the plasma is the combined result of the electron $\lambda_e \nabla T_e$ and ion $\lambda_i \nabla T_i$ activity, where λ is the conductivity coefficient and T is the temperature. The radiation transport process is represented here as flux $\mathbf{S}_{rad}$ and the laser heating source as Q_{las}. Also taken into account is the energy interchange between electrons and ions in the form $3\frac{m_e n_e}{m_i \tau_e}\left(k_B T_e - k_B T_i\right)$ [12] and the thermally generated magnetic field $\frac{ck_B}{en_e}\nabla n_e \times \nabla T_e$ [13, 14]. Here m is the mass; n_e and τ_e are electron concentration and the relaxation time; c – speed of light; e – electron charge; and k_B – Boltzmann constant. To complete this full set of MHD equations, functions for the thermodynamic pressure of electrons $p_e = p(e_e, \rho)$, resistivity $\eta = \eta(e_e, \rho)$, and thermal conductivity $\lambda_{e/i} = \lambda(e_{e/i}, \rho)$ are determined from the equation of state, discussed in [2]. Equation (1) constitutes the initial set of equations used for modeling laser generated plasma processes. The conditions of a particular problem and a specific geometry will lead to the transformation of the main equations. If the EUV device and plasma motion does not have symmetry, we expressed Eq. (1) in the 3-D Cartesian coordinate system otherwise, the 2D cylindrical coordinate system can be used. Since the final set of the transformed equations has convective terms (hydrodynamic flux) and dissipative terms (heat conduction, laser heating, radiation transport, and electron-ion interaction), we used splitting of physical processes in our numerical algorithm to separate the hyperbolic and parabolic parts [4]. The conservative form of the initial equations allows the use of the TVD method in the Lax-Friedrich formulation (TVD-LF) for solution of the convective stage. An implicit numerical scheme with sparse matrix linear solvers is used for calculating the heat conduction and magnetic diffusion terms [4, 15]. The Monte Carlo methods are used for modeling the radiation processes: laser heating, photon radiation transport in the plasma, and the EUV output [2, 4].

Interaction between separate particles underlies all effects that occur by interaction various particles with matter. The physical model that can be used for description of the plasma debris motion should be constructed on consideration of the separate interactions of beam particles with the target particles. This is well known approximation of pair collisions [16]. It is supposed in this approximation that the bullet particle is interacting simultaneously only with one particle of the target (nucleus or electron). Interaction is occurring in one point and instantly. The developed Monte Carlo model in this paper is based on this principle and assumes that energetic particles are remote from each other at distance larger than Coulomb shielding of the target. These assumptions allow introducing the conception of the particle trajectory as a

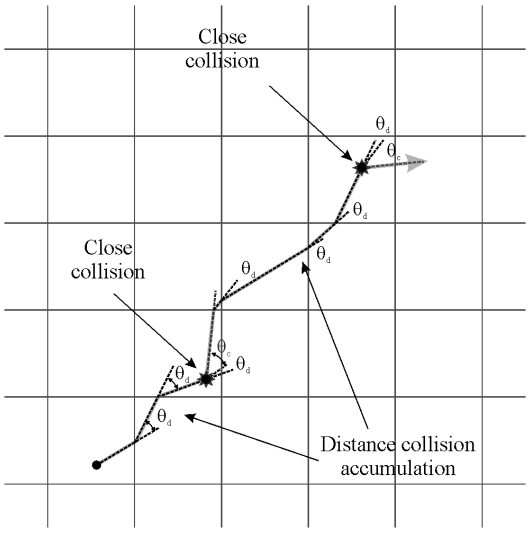

Fig. 1. Monte Carlo model of ion collisions

line of combined sections between separate interactions (Fig. 1). Energy and momentum of the particle is changing at the points of interactions. Because initial energy of the fast ions does not exceed 50 keV non-elastic scattering are not included for this analysis. HEIGHTS package considers detailed Monte Carlo model of elastic scattering. Because we can not take into account all separate interactions of energetic particles with the target atoms (limited computer abilities), all impacts is separated on two groups: close collisions and distant collisions. Criterion for developed separation is the energy which is transmitted to the recoiled particle. It is assumed in this model that all interactions where particle loses energy part smaller than 10^{-2} are distant. The distant interaction results are accumulating on the trajectory and should be added along the moving particle way. Accordingly described principle, our developed Monte Carlo model can be related to the class of the small energy transfer grouping methods. Following the developed physical model, the fast ions of the EUV source debris can interact with the nucleuses and electrons of the chamber gas in the distant and close interactions. Initial data for the calculations start is a density field of the target gas and a source energy distribution of the fast ions. The interactions of the fast ions with the chamber gas nucleuses were calculated using the approximation of the Thomas-Fermi potential

$$\left(\frac{d\sigma}{dT}\right)_n = \frac{C_m}{E^m T^{1+m}}, \text{ for potential form} \tag{2}$$

$$V(r) = \frac{Z_1 Z_2 e^2}{r}\chi\left(\frac{r}{a_{TF}}\right). \tag{3}$$

Here E – initial energy of the fast ion; T – transmitted to recoil particle energy; Z – charge of nucleus; subscript 1 refer to the incident energetic particle and 2 to the recoil particle.

$$C_m = \frac{1}{2}\pi\lambda_m a_{TF}^2\left(\frac{M_1}{M_2}\right)^m\left(\frac{2Z_1 Z_2 e^2}{a_{TF}}\right)^{2m}, \tag{4}$$

$$a_{TF} = \frac{1}{2}\left(\frac{3\pi}{4}\right)^{2/3}\frac{\hbar^2}{m_e e^2}(Z_1^{2/3} + Z_2^{2/3})^{-1/2}, \text{ where} \tag{5}$$

coefficients m and λ_m depend from energy of fast ion and given by: $E \geq 1MeV$, $m = 1$, $\lambda_1 = 0.5$ (Rutherford scattering); $100keV < E < 1MeV$, $m = \frac{1}{2}$, $\lambda_{1/2} = 0.327$ (major portion of the keV range); $E \leq 100keV$, $m = \frac{1}{3}$, $\lambda_{1/3} = 1.309$ (lower-keV and upper-eV region).

By the defined stopping power for energies under the close-distant border $T_* < 0.01E$

$$\left(\frac{dE}{dx}\right)_n = N_n\int_{T_d}^{E} T d\sigma = N_n\frac{C_m}{E^m}\frac{1}{1-m}\left(T_*^{1-m} - T_d^{1-m}\right) \tag{6}$$

we can find the energy loss ΔE on the elementary path l

$$\Delta E = l\left(\frac{dE}{dx}\right)_n, \text{ where} \tag{7}$$

T_d is the energy for the displacement of the target atom (zero for gas). Close nucleus collision part can be calculated by integration of the differential cross-section Eq. (2) on energies from T_* border up to maximum possible energy that can be transmitted to the nucleus

$$T_{\max} = \frac{4M_1M_2}{(M_1+M_2)^2}E: \tag{8}$$

$$\sigma_{in} = \int_{T_*}^{T_{\max}} \left(\frac{d\sigma}{dT}\right)_n dT = \frac{C_m}{m}\frac{1}{E^m}\frac{T_{\max}^m - T_*^m}{T_{\max}^m T_*^m}. \tag{9}$$

Differential cross section of energy transfer from ion to electron for high-energy ions is given by [17]

$$\left(\frac{d\sigma}{dT}\right)_e = \frac{2\pi Z_{eff}^2 m_e r_e^2}{\beta^2}\left(1-\beta^2\frac{T}{T_{\max}}\right)\frac{1}{T^2}, \text{ where} \tag{10}$$

$\beta = v_i/c$ – fast ion velocity normalized on speed of light; $r_e = \frac{e^2}{m_e c^2}$ – classical radius of electron; and effective ion charge can be obtained from

$$Z_{eff} = Z_1\left(1-1.034\exp\left(-137.04\beta/Z_1^{0.69}\right)\right). \tag{11}$$

By the applying of (8) or relativistic expression from [17] to calculation of the maximum possible transmitted energy from the fast ion to separate electron it is obvious to see that this energy is very small, i.e. $T_{\max} << 0.01E$. As a result fast ions deceleration is considered in distant collisions only. Close collisions of ions with separate electrons is only important in the case of very high energy ions (not for the lithography case) for the study of secondary effects. The secondary effects include occurrence of high energy recoil electron. HEGHTS models in general describe such interaction using the total cross-section

$$\sigma_{ie} = \int_{T_*}^{T_{\max}} \left(\frac{d\sigma}{dT}\right)_e dT = \frac{2\pi Z_{eff}^2 m_e r_e^2 c^2}{\beta^2}\left[\frac{T_{\max}-T_*}{T_{\max}T_*} - \frac{\beta^2}{T_{\max}}\ln\left(\frac{T}{T_{\max}}\right)\right]. \tag{12}$$

The model of distant collisions of fast ions with electrons is more complicated because two approximations should be used for interaction description [18]: Bethe theory for high energy of the incident energetic ions

$$\left(\frac{dE}{dx}\right)_{ie,B} = \frac{2\pi Z_{eff}^2 Z_2}{\beta^2} N_n m_e r_e^2\left[\ln\left(\frac{2m_e c^2\beta^2\gamma^2 T_*}{I^2}\right) - \beta^2\left(1+\frac{T_*}{T_{\max}}\right)\right] \tag{13}$$

and Linhard stopping power for low energy ions

$$\left(\frac{dE}{dx}\right)_L = C_L\sqrt{E}, \text{where} \tag{14}$$

$\gamma^2 = \dfrac{1}{1-\beta^2}$; I – average ionization potential; $C_L = K\left(E_L / 1.602\cdot 10^{-9}\right)^{1/2} / \left(R_L \cdot 10^4\right)$ $\left(KeV^{1/2}/\mu m\right)$;

$E_L = (1+A)Z_1 Z_2 e^2/(Aa)$ [erg]; $a = 0.4683\left(Z_1^{2/3} + Z_2^{2/3}\right)^{-1/2}\cdot 10^{-8}$ [cm]; $R_L = (1+A)^2/4\pi A N_n a^2$ [cm];

$A = A_2/A_1$ – atomic weights of nucleuses; $K = \dfrac{0.0793 Z_1^{2/3} Z_2^{1/2}(1+A)^{3/2}}{\left(Z_1^{2/3} + Z_2^{2/3}\right)^{3/4} A_2^{1/2}}$; N_n - target atom number density.

Especially for the presented model was developed fitting function for the continuous combining of both models. Fitting function is given by

$$\left(\frac{dE}{dx}\right)_{Fit} = \left(\frac{dE}{dx}\right)_L e^{-\sqrt{FIT}} + \left(\frac{dE}{dx}\right)_B \text{ with} \qquad (15)$$

$$FIT = \frac{2m_e c^2 \beta^2 \gamma^2 T_{\max}}{I^2} + 1.$$

Based on the described models of fast ions interaction the Monte Carlo algorithm is developed for the calculation of fast ions deceleration in the chamber gas. The algorithm takes into account consideration of the secondary (recoiled) particles, if the energy of these particles is higher than a critical value. This assumption allows accurate calculations of

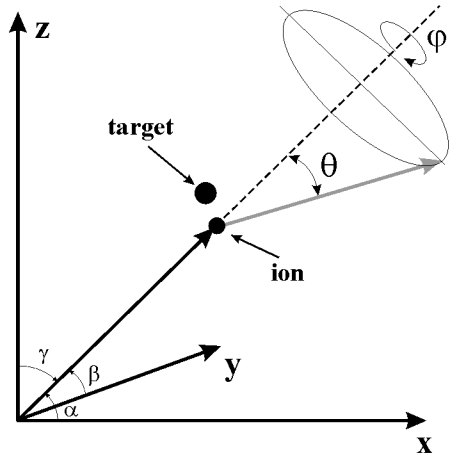

Fig. 2. 3D scattering scheme of the fast ion on the target nucleus

the energy transport in system fast ions beam–target gas. Figure 2 presents schematically scattering of the fast ion by the target particle with angles θ and φ.

New directional cosines after interaction is given by the formula

$$\cos\alpha' = \cos\alpha\cos\theta + (\cos\alpha_r - \cos\alpha\cos\theta_r)\sqrt{\left(1-\cos^2\theta\right)/\left(1-\cos^2\theta_r\right)}$$

$$\cos\beta' = \cos\beta\cos\theta + (\cos\beta_r - \cos\beta\cos\theta_r)\sqrt{\left(1-\cos^2\theta\right)/\left(1-\cos^2\theta_r\right)}, \text{ where} \qquad (16)$$

$$\cos\gamma' = \cos\gamma\cos\theta + (\cos\gamma_r - \cos\gamma\cos\theta_r)\sqrt{\left(1-\cos^2\theta\right)/\left(1-\cos^2\theta_r\right)}$$

$\alpha_r, \beta_r, \gamma_r$ – angles of random direction; and θ_r – angle between ion initial and random directions.

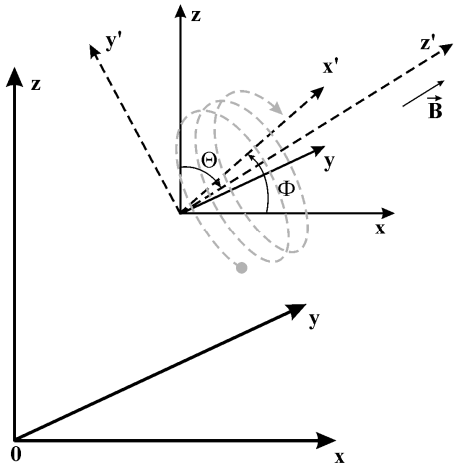

Fig. 3. Trajectory of the fast ion in the case of external magnetic field and coordinate system relationship

External magnetic field was used in the fast ions mitigation system for two purposes: as instrument of the extension of the ion way through damping matter and as redirector of ions, i.e., reflector system to safe location away from the optic collector system. Implementation of the magnetic field to the developed Monte Carlo model allows the modification of free fly trajectories between scattering (Fig. 3). The charged particle drifts in the external magnetic field with Larmor radius along the force line between scatterings. The Monte Carlo model demands using an equation set of particle motion where coordinate and velocity directions are functions not in time, but in the path s. So equations can be easily obtained in the coordinate system S' where z'-axis is parallel magnetic field $\mathbf{B}$:

$$
\begin{aligned}
x' &= x'_0 + \operatorname{sgn}(q_i)\frac{|\mathbf{v}|}{\omega_{\mathbf{L}}}\cos\beta'_0 + \frac{|\mathbf{v}|}{\omega_{\mathbf{L}}}\sin\gamma'_0\cos\left[-\operatorname{sgn}(q_i)\frac{\omega_{\mathbf{L}}}{|\mathbf{v}|}s+\varphi'\right] \\
y' &= y'_0 - \operatorname{sgn}(q_i)\frac{|\mathbf{v}|}{\omega_{\mathbf{L}}}\cos\alpha'_0 + \frac{|\mathbf{v}|}{\omega_{\mathbf{L}}}\sin\gamma'_0\sin\left[-\operatorname{sgn}(q_i)\frac{\omega_{\mathbf{L}}}{|\mathbf{v}|}s+\varphi'\right] \\
z' &= z'_0 + s\cos\gamma'_0 \qquad \text{, where} \qquad (17) \\
\cos\alpha' &= \operatorname{sgn}(q_i)\sin\gamma'_0\sin\left[-\operatorname{sgn}(q_i)\frac{\omega_{\mathbf{L}}}{|\mathbf{v}|}s+\varphi'\right] \\
\cos\beta' &= -\operatorname{sgn}(q_i)\sin\gamma'_0\cos\left[-\operatorname{sgn}(q_i)\frac{\omega_{\mathbf{L}}}{|\mathbf{v}|}s+\varphi'\right] \\
\cos\gamma' &= \cos\gamma_0
\end{aligned}
$$

q_i – charge of ion; α', β' and γ' – directional angles of the particle velocity in S' system; the way $s' = s$ is equal in the auxiliary system S' and initial laboratory system S. The Larmor frequency can be given by

$$\omega_{\mathbf{L}} = \frac{|q_i||\mathbf{B}|}{m_i c}. \qquad (18)$$

3. VALIDATION AND BENCHMARKS

The hydrodynamics, radiation transport, heat conduction, and EUV benchmarks of previous simulations are described elsewhere [2-4, 15, 19]. Here we present validation of the developed physical model and the Monte Carlo numerical simulation of fast ions interaction with the chamber gas. The developed package was tested in wide range of energy of the incident fast ions. We also tested the range for the joint action of the two approaches: Bethe (13) and Linhard (14). For this reason HEIGHTS calculation were compared with available experimental and theoretical data for ion energies between 17 keV and 1.2 MeV. In the low energy case we calculated the Li^+ ions energy distribution after transmission through 14 nm Cu film [20]. Initial energy of the Li^+ ions was 17 keV. Figure 4a presents comparison of our calculations with experimental data [20]. As it can be seen, good correspondence with the experimental data is obtained.

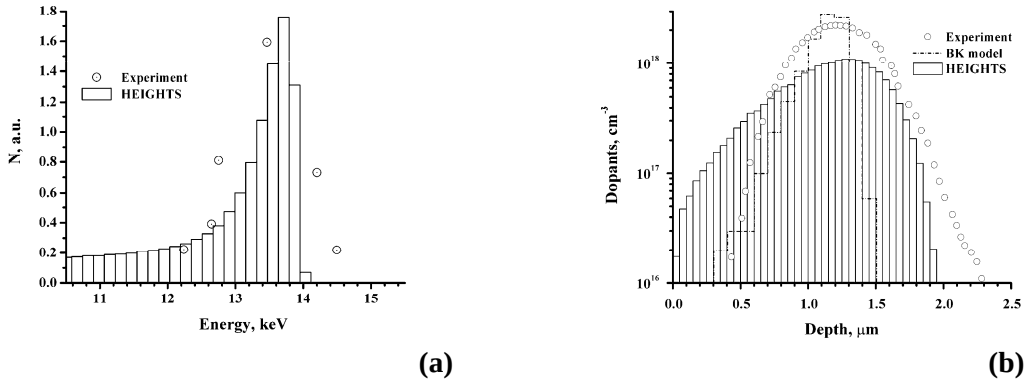

Fig. 4. Comparison of HIEGHTS calculations and experimental data:
a) energy distributions of the 17 keV Li^+ ions after transmission through 14 nm Cu film [20];
b) The depth distributions of P^+ dopant in Si substrate. Initial energy of dopant 1.2 MeV, implantation dose $1 \cdot 10^{14}$ cm^{-2}. Experimental [21] and theoretical [22] data.

In the high energy range, HEIGHTS benchmarking is compared with both the experimental [21] and the theoretical [22] data of 1.2 MeV P^+ ions implantation into Si substrate. The comparison was made for the depth distributions of dopant (implantation dose $1 \cdot 10^{14}$ cm^{-2}). Figure 4b shows good correspondence of HEIGHTS calculations to the published experimental and numerical data. This is an additional confirmation of the validity of HEIGHTS theoretical model and integrated numerical methods to the study of mitigation processes for EUV lithography.

4. NUMERICAL RESULTS

In [3, 23-24] we published our continuing progress in modeling and optimization of the DPP devices. Here we present further calculations for development and optimization of LPP devices, combined LPP+DPP devices, and the debris mitigation devices. Our calculations were carried out for the both xenon and tin plasmas. Here we present our numerical modeling of the tin target material because of its current interest as the source for 13.5 nm EUV lithography. Many investigators are trying to optimize the tin target geometry, laser pulse and prepulse characteristics, and device chamber design in order to increase the EUV output source efficiency, to mitigate the debris, and to improve the manufacturability of the whole process. An ideal light source for the EUV lithography is a small spherical target with high enough density and with optimum temperature for maximum EUV output. This approach is used in many theoretical investigations to study the efficiency of the EUV emission and source improvement. In reality, the EUV emission region is only a thin layer between regions with high temperature and low density and regions with high

density and low temperature. The size and form of the EUV region depend on many factors, such as target material, target structure, laser beam parameters, and spatial configuration of the LPP device. Enlarging and shaping of this region will enable researchers to increase the LPP device efficiency and to develop the required high EUV power source for lithography. Our objective here is to use multiple laser beams to initiate hydrodynamic confinement of the expanding laser plasma and to increase the total EUV radiation zone. The multiple laser beams compared to a single laser beam with the same total energy can yield higher EUV efficiency. Moreover, the optimal locations and angle of incidence of the laser beams can be obtained for various target geometries. We focused our simulations on two generally used target geometries: a droplet target and a plane target (Fig.5). A three-beam configuration of the LPP devices was selected for our numerical simulation because of the small number of spatial orientation parameters (needed for optimization) and the good potential for plasma confinement [25]. HEIGHTS, however, can handle any number of incident laser beams.

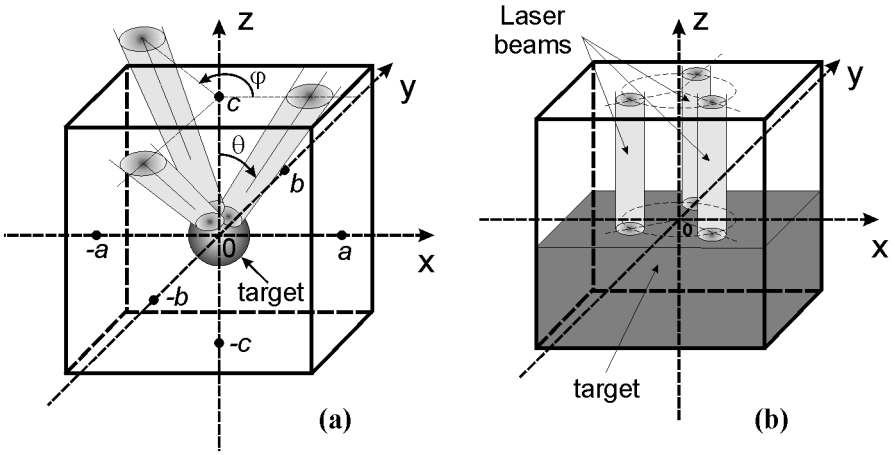

Fig. 5. Schematic illustration of multiple laser beam devices: a) with droplet target; b) with plane target.

Based on latest published experiments and our preliminary calculations, [4, 26, 27] we used the following initial parameters for the single-beam droplet target device: a spherical tin target with a 100 μm diameter, a laser pulse with a total energy of up to 230 mJ, and duration of 10 ns. The plane target is more conventional, easy to use, and is better examined in laser plasma experiments. We based our plane tin target simulations on the experimental work described in details in Ref. [28]. Following this paper, we used radius $\sigma_s = 1.49 \cdot 10^{-2}$ cm for the single laser beam Gaussian distributed in space. As in droplet target case, the time shape of pulse was square and the optimum laser wavelength was 1064 nm. Duration of the laser pulse was taken equal to 7.5 ns.

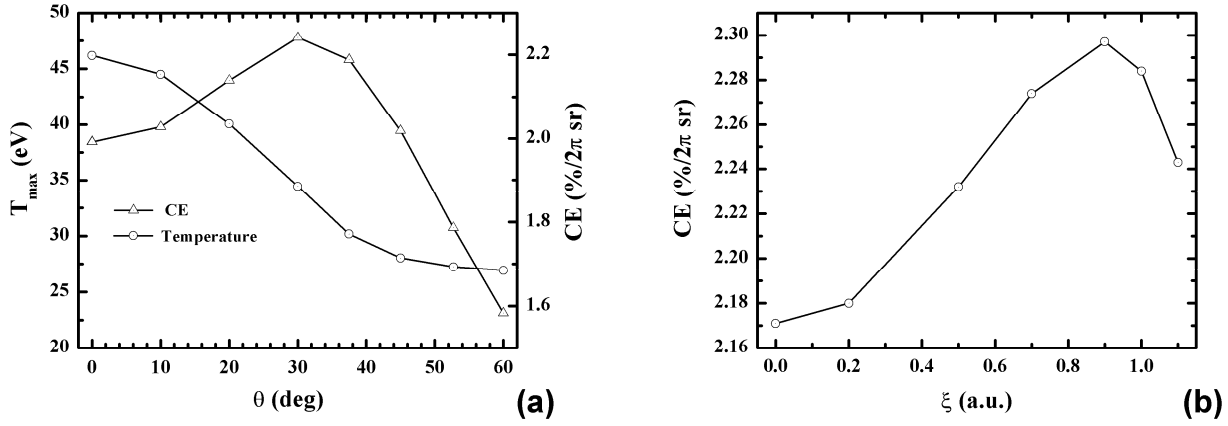

Fig. 6. Optimization of multi-laser device conversion efficiency: a) axial angle dependence for droplet target device; b) laser beam displacement ratio dependence for plane target device [25].

The total laser radiation energy of 0.3 J on the target surface produced an irradiance level of $5.73 \cdot 10^{10}$ W/cm^2. As it shown experimentally [28] and confirmed in our calculation, this is the optimum conditions for EUV output at normal incidence of laser beam on target surface. Figure 6a shows the dependence of conversion efficiency (CE) on the axial angle for the three laser beams system with total laser energy of 45 mJ. The maximum temperature in the computational domain is presented just to show the redistribution of plasma parameters, i.e., areas with low density are not overheated as in the single-beam case. As shown, the maximum CE was obtained at an axial angle of $\theta \approx 30^{\circ}$. The value of the CE was increased from 2.0 %/2π sr for the single-beam case up to 2.24 %/2π sr. The optimization parameter for the plane target was expressed as the beams displacement ratio $\xi = R_1/R_0$, where R_0 is the laser beam radius and R_1 is the laser beams bundle radius. The case $\xi = 0$ corresponds to the basic single-beam LPP device, and following our prediction, there should exist a displacement ratio $\xi > 0$ such that $CE(\xi) > CE(0)$. Figure 6b shows the dependence of the final EUV conversion efficiency on the displacement ratio. The CE reaches a maximum value at ξ - ratio equal ~ 0.9 and was increased from 2.17 % up to 2.30%. The increase in the CE can be higher for different laser beams configurations, for example by pyramidal arrangement of laser beams under the plane target surface. In these cases more than one optimization parameter exist and these numerical simulations are being considered in our future work.

The recent simulation experimental data combining both LPP and DPP devices was used for construction and optimization of the hybrid LPP+DPP device [29]. Figure 7 presents device where initial plasma is produced with a laser beam on tin cathode surface of the DPP device. The expanded laser plasma should be optimally compressed with the discharge for the highest EUV radiation generation.

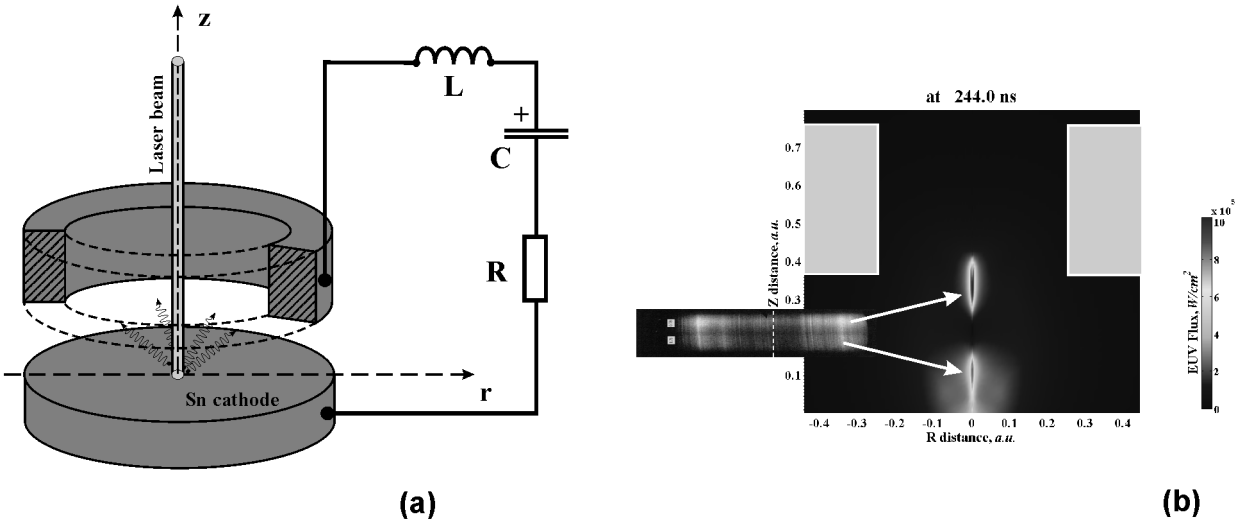

Fig. 7. DPP+LPP hybrid device: a) schematic illustration; b) two areas of pinching obtained in HEIGHTS simulations (background) and in the experimental data [29].

Our HEIGHTS numerical simulation successfully produced the two pinch areas of the intense EUV radiation generation in this hybrid device with the specific initial parameters of the laser prepared plasma. These two EUV areas (near cathode and near anode) were observed in experiment Ref. [29].

HEIGHTS can also be used to simulate and optimize debris mitigation systems. It is very expensive to use laboratory experiments for optimizing the mitigation system. We used HEIGHTS on a sample of mitigation device that can be optimized to work with actual EUVL source devices. The behavior of the charged particles in the chamber gas was considered separately from that of the neutral particles in approximation of pair collisions. Damping capabilities of the chamber gas are important not only for energy decrease at the mirror surface, but also for the magnetic field control and deflection of the charged particles. An actual reduction of the ion velocity follows from a decrease of the Larmor radius; as a result, slower particles can be easily deviated to a safe area. The simulated results indicate that heavy ions can be decelerated more effectively than light ions. However, in actual cases of lithographic plasmas, the light ions have lower initial energy than heavy ions. We proposed to use a magnetic field with gas jet to improve the mitigation of charged

particles. Such a mitigation system is presented schematically in Fig. 8. As it shown, escaping debris was detected in spherical surface around the mitigation device. This simulation allows registration of neutral and charged particles deviations in all directions. Fast ions of Sn were tested as the main debris. The initial energy distribution of the fast Sn ions was taken from actual experimental data [30]. The test calculations were made for magnetic field magnitudes of 0, 0.1, 0.5, and 1 T in He or Ar chamber gas. The energy and location distributions of the ions at the detector sphere (5 cm around debris source) were registered and normalized to the solid angle.

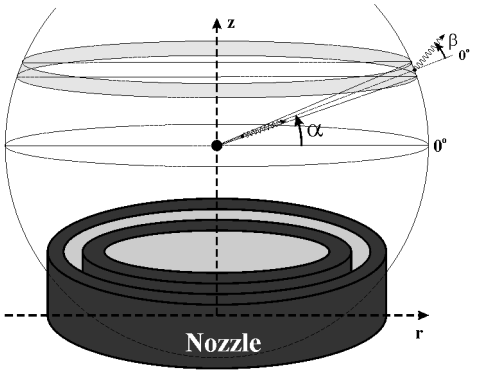

Fig. 8. Schematic illustration of the debris mitigation detector

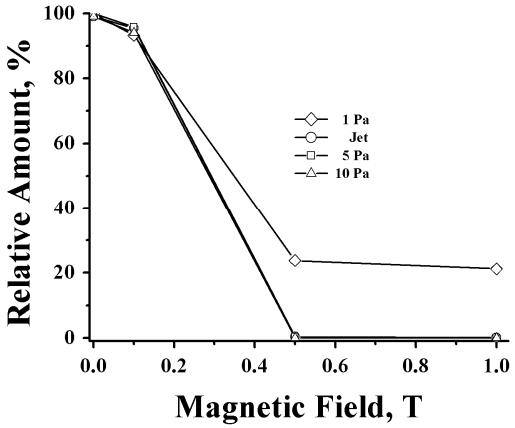

Fig. 9. Relative amount (in comparison to initial flux) of fast ions in x-y plane direction at 5 cm distance as function of external magnetic field. Various He chamber gas pressure with Sn particles.

We found that the external magnetic field is very useful for redirecting charged particles (Fig. 9). At the same time, the magnetic field has little effect on the kinetic energy of particles. The size of the Larmor radius for this condition was comparable with the device size, and the path of the particles was not significantly increased. The Larmor radius is a critical parameter for the present problem. A smaller radius leads to a more effective deviation of ions with the magnetic field. Decreasing the ion velocity decreases the Larmor radius as well. Ion velocity can be decreased with increased chamber gas density. As a consequence, the mitigation system should be optimized for the following plasma source parameters: geometry, size, distance to the reflection system, and working gas properties. A safe location for the decelerated debris can be determined from the calculated directional debris distributions of the mitigation system.

5. CONCLUSIONS

The developed integrated and benchmarked models in HEIGHTS package can simulate in great details DPP, LPP, hybrid DPP+LPP, and debris mitigation devices. Optimization of various device parameters was carried out in wide range. Optimization of hydrodynamic plasma confinement processes is proposed for increasing the conversion efficiency of the LPP. Further investigations of the effect of plasma confinement on the final CE of LPP devices should involve optimization of initial parameters: laser beam arrangement in space, laser power density distribution in time and in cross-section of beam, laser pulse duration, target geometry, and target structure.

Physical models were also developed for simulating the main processes that occur in EUV lithography mitigation systems: gaseous jet propagation in the chamber, removal of neutral particles and macroscopic droplets with the gaseous jet, and deviation of charged particles in a magnetic field. Various geometries of the mitigation system were considered for debris removal by the EUV lithographic process. Other mitigation geometries can be easily accommodated. Xe, Li, and Sn debris in Ar and He gaseous jets were analyzed using the developed HEIGHTS simulation package. Attenuation of EUV flux by propagation through neutral chamber gas was calculated for He and Ar. A 3-D Monte Carlo model of ion propagation in the chamber gas was also developed. The initial distributions of fast ions were derived from experimental data. Sn ion mitigation was modeled with and without an external magnetic field.

ACKNOWLEDGMENTS

Part of this work was supported by SEMATECH and the Intel Corporation. Argonne National Laboratory's work was supported by the U.S. Department of Energy, under contract DE-AC02-06CH11357.

REFERENCES

1. V. Bakshi, "EUV Source Technology: Challenges and Status" in *EUV Sources for Lithography*, edited by V. Bakshi (SPIE Press, Bellingham, Washington USA, 2006).
2. A. Hassanein, V. Sizyuk, V. Tolkach, V. Morozov, and B. J. Rice, "HEIGHTS initial simulation of discharge produced plasma hydrodynamics and radiation transport for extreme ultraviolet lithography," *Journal of Microlithography, Microfabrication, and Microsystems*, 3, 130-138 (2004).
3. A. Hassanein, V. Sizyuk, V. Tolkach, V. Morozov, T. Sizyuk, B. J. Rice, and V. Bakshi, "Simulation and optimization of DPP hydrodynamics and radiation transport for EUV lithography devices," *Proceedings of SPIE*, 5374, 413-422 (2004).
4. V. Sizyuk, A. Hassanein, V. Morozov, V. Tolkach, T. Sizyuk, "Numerical simulation of laser-produced plasma devices for EUV lithography using the heights integrated model," *Numerical Heat Transfer, Part A*, 49(3), 215-236 (2006).
5. G. Tóth and D. Odstrčil, "Comparison of some flux corrected transport and total variation diminishing numerical schemes for hydrodynamic and magnetohydrodynamic problems, " *J. Comp. Phys.*, 128, 82-100 (1996).
6. R. Leveque, *Finite volume methods for hyperbolic problems*, 64-127, Cambridge, (2002).
7. R. Siegel and J. R. Howell, "Radiation transfer with absorbing, emitting, and scattering media," in *Thermal Radiation Heat Transfer, v. III*, chap. 6, NASA, Washington, (1971).
8. K. C. Kannenberg and I.D. Boyd, "Strategies for efficient particle resolution in the direct simulation Monte Carlo method," *J. Comp. Phys.*, 157, 727-745 (2000).
9. V. Tolkach, A. Hassanein, and V. Morozov, *Development of comprehensive models for opacities and radiation transport for IFE system*, Argonne National Lab. Rep. ANL-ET/02-23, Argonne, IL (2002).
10. K. Takenoshita, C.-S. Koay, S. Teerawattansook, M. Richardson, and V. Bakshi, "Ion emission characterization from microscopic laser-plasma Sn -doped droplet sources," 3rd International Extreme Ultraviolet Symposium, 1-4 November, Miyazaki, Japan (2004).
11. D. Ruzic et al., "Measurement and modeling of energetic ions from a commercial EUV Z-pinch," 6th International Conference on Dense Z-Pinches, Oxford, UK, July, 26 (2005).
12. S. Braginskii, "Transport Properties in a Plasma," in *Reviews of Plasma Physics*, edited by M.A. Leontovich (Consultants Bureau, New York), 1, 205 (1965).
13. S.R Goldman, and R.F. Schmalz, "Magnetic field behavior beyond the laser spot," *Phys. Fluids*, 30, 3608 (1987).
14. P. Mora, "Magnetic field generation in the underdense plasma," *Phys. Fluids*, 24, 2219 (1981).
15. V. Miloshevsky, V. Sizyuk, M. Partenskii, A. Hassanein and P. Jordan, "Application of finite-difference methods to membrane-mediated protein interactions and to heat and magnetic field diffusion in plasmas," *J. Comp. Phys.*, 212, 25 (2006).
16. B.B. Kadomtsev, "About the active field in plasma," *JETP*, 33, 151 (1957).
17. V. Berestetskii, E. Lifshits, L. Pitaevskii, *Quantum electrodynamics*, Oxford, New York (1982).
18. T.A. Mehlhorn, "A finite material temperature model for ion energy deposition in ion-driven inertial confinement fusion targets," *J. Appl. Phys.*, 52, 6522 (1981).
19. V. Sizyuk, A. Hassanein, V. Morozov, and T. Sizyuk, *Heights Integrated Model as Instrument for Simulation of Hydrodynamic, Radiation Transport, and Heat Conduction Phenomena of Laser-Produced Plasma in EUV Applications*, Argonne National Lab. Report ANL-MCS-CPH-06/56, Argonne, IL (2006).
20. E. Zarutskii, *Physics of the Solid State*, 9, 1896 (1967).
21. D.C. Ingram, and J.A. Baker, "Range distributions of MeV implants in silicon," *Nucl. Instr. and Meth.*, B7/8, 361 (1985).
22. M. Posselt and W. Scorupa, "The electronic stopping and range profile calculations for high energy implantation of phosphorous into silicon," *Nucl. Instr. and Meth.*, B21, 8 (1987).

23. A. Hassanein, V. Sizyuk, V. Tolkach, V. Morozov, and B.J. Rice, "HEIGHTS initial simulation of discharge-produced plasma hydrodynamics and radiation transport for EUV lithography", *Proceedings of SPIE.*, 5037, 714-727 (2003).
24. A. Hassanein, V. Morozov, V. Sizyuk, V. Tolkach, and B.J. Rice, "HEIGHTS-EUV package for DPP source modeling," in *EUV Sources for Lithography*, edited by V. Bakshi (SPIE Press, Bellingham, Washington USA, 2006).
25. V. Sizyuk, A. Hassanein, and T. Sizyuk, Three-dimensional simulation of laser-produced plasma for extreme ultraviolet lithography applications, *J. Appl. Phys.*, 100(10), 103106 (2006).
26. M. Richardson, C.-S. Koay, K. Takenoshita, C. Keyser, and M. Al-Rabban, "High conversion efficiency mass-limited Sn-based laser plasma source for extreme ultraviolet lithography," *J. Vac. Sci. Technol. B,* 22, 785 (2004).
27. S.S. Harilal, B. O'Shay, M.S. Tillack, Y. Tao, R. Paguio, A. Nikroo and C.A. Back, "Spectral control of emissions from tin doped targets for extreme ultraviolet lithography," *J. Phys. D: Appl. Phys.*, 39**,** 484 (2006).
28. R.C. Spitzer, T.J. Orzechowski, D.W. Phillion, R.L. Kauffman, and C. Cerjan, "Conversion efficiencies from laser-produced plasmas in the extreme ultraviolet regime," *J. Appl. Phys.*, 79, 2251 (1996).
29. K. Koshelev, V. Bakshi "Benchmarking Modeling of DPP EUV Sources." Presentation on EUV Source Workshop, Vancouver, May 25 (2006).
30. K. Takenoshita, C.-S. Koay, S. Teerawattansook, M. Richardson, and V. Bakshi, "Ion emission characterization from microscopic laser-plasma tin-doped droplet sources," Presentation on the *3rd International Extreme Ultraviolet Symposium*, 1-4 November, Miyazaki, Japan, (2004).